Article

Not peer-reviewed version

A Comparative Study of Sol-Gel Deposited Zinc Oxide, Tin Oxide, and Titanium Dioxide Thin Films and Their Photocatalytic Performance on MB Decoloration

Heberto Gómez *, Angélica Gómez-Monsivais, Krishna Karthik Tangirala, Hector Daniel Molina, Maria De la Luz Olvera, Arturo Maldonado, Jose Luiz González

Posted Date: 11 September 2024

doi: 10.20944/preprints202409.0880.v1

Keywords: photocatalysis; methylene blue; thin film; dip coating

Article

A Comparative Study of Sol-Gel Deposited Zinc Oxide, Tin Oxide, and Titanium Dioxide Thin Films and Their Photocatalytic Performance on MB Decoloration

Angélica Gómez-Monsivais [1], Tangirala Venkata Krishna Karthik [2], H.D. Molina-Ruiz [3], María de la Luz Olvera [1], Arturo Maldonado [1], José Luis González Vidal [3] and Heberto Gómez-Pozos [3,*]

[1] SEES, Departamento de Ingeniería Eléctrica, Centro de Investigación y de Estudios Avanzados del Instituto Politécnico Nacional, CINVESTAV-IPN, 07000 México City, México
[2] Tecnologico de Monterrey, School of Engineering and Sciences, Department of Mechanics and Advanced Materials, Avenida Lago de Guadalupe KM 3.5, Margarita Maza de Juárez, 52926 Lopez Mateos city, Mexico
[3] Área académica de computación y electrónica, Universidad Autónoma del Estado de Hidalgo, 56092 Pachuca, Hidalgo, México
* Correspondence: gpozos@uaeh.edu.mx; Tel.: +527-717-172-000 (ext. 2234 or 2235).

Abstract A comparative study of the photocatalytic decoloration of methylene blue (MB) dissolved in water was conducted, using three semiconductor oxides: zinc oxide (ZnO), tin oxide (SnO_2) and titanium dioxide (TiO_2) in the form of thin films and varying their thickness ~ 100, 200, and 300 nm for each film. All the films were deposited using the cost-effective dip-coating technique, at moderate temperature processing (400 °C) with sol-gel solutions on cheap glass substrates. The structural, morphological, and compositional properties of the films were analyzed by X-ray Diffraction (XRD), Scanning Electron Microscopy (SEM), and Raman spectroscopy, respectively. The degradation of MB was studied by varying both thickness and type of semiconductor oxides through measurements of optical absorbance of decolorated liquid by photocatalytic process. Structural analysis shows that ZnO and SnO_2 films were polycrystalline with preferential growth of (002) and (110) planes respectively, whereas, an amorphous structure was observed for TiO_2 films. In addition, morphological properties confirms that the surfaces of all the films are conformed with nano grains in round and irregular shapes. Based on all results reported in this work, that authors believe that the degradation efficiency of MB depends on the thickness of the film and the type of semiconductor material used as a catalyst. The highest degradation efficiencies were recorded with an exposure time of 120 min and with an initial concentration of 10 mg/L for ZnO, SnO_2, and TiO_2 films were: 100, 88 %, and 76 %, respectively.

Keywords: photocatalysis; methylene blue; thin film; dip coating

1. Introduction

Water and air pollution represent significant challenges for all forms of life, exacerbated by industrial growth, rising energy demands, and rapid population expansion. In particular, the textile industry has seen an unprecedented surge in activity, contributing notably to water pollution. The waste products generated during the dyeing process of fabrics are frequently released into natural water bodies without adequate oversight regarding their impact on these vital resources, thereby negatively affecting the health of various organisms. Presently, it is estimated that approximately 70% of the water utilized in dyeing processes is discharged into aquatic ecosystems without any prior treatment, leading to the emergence of carcinogenic diseases and harmful mutagenic effects on both

 doi:10.20944/preprints202409.0880.v1

aquatic life and humans. [1]. Additionally, dyes have low fixation on factory-made goods requesting higher concentration for better fixation, resulting in dye concentrations wastes in rivers exceeding 1500 mg/L. During dyeing processes, various toxic substances are emitted, including salts such as NaCl and Na_2SO_4, surfactants like phenols and amines, heavy metals found in dyes, chlorinated solvents, harmful anions such as sulfide, and various colored organic compounds [2]. The by-products generated throughout these processes exhibit significant toxicity and possess low biodegradability. It is reported that only 45 to 47 percent of the dyes utilized are biodegradable [3], with the remaining color primarily attributed to insoluble dyes, which further contributes to their low biodegradability. In order to address these problems, complex and costly water treatment techniques have been developed, such as filtration, electro flocculation, reverse osmosis, among others, with limited efficiency when applied on a large scale [4–6]. Usual and new pollutant chemically stable species are difficult to treat with conventional methods, hence innovative, effective, environmentally friendly, and cost-effective processes are required to ensure a higher percentage of contaminant removal or degradation. In recent years, advanced oxidation processes (AOPs) have garnered significant attention due to their environmentally friendly approach to eliminating and degrading water pollutants. These processes generate reactive chemical species, primarily hydroxyl radicals (OH) and superoxide anions (O^{*-}), which interact with contaminants to form less harmful byproducts, including inorganic precipitates, carbon dioxide (CO_2), and water (H_2O). AOPs typically utilize heterogeneous photocatalysis with semiconductor oxides like titanium dioxide (TiO_2), zinc oxide (ZnO), tin dioxide (SnO_2), and tungsten trioxide (WO_3), among others. [7–13]. Semiconductor oxides can be manufactured in thin film or powder form and can be processed by both physical and cost-effective chemical techniques, including sol-gel by dip coating or spinning, chemical bath, spray pyrolysis, among others [14–16]. The sol-gel is an attractive and economical deposition chemical technique since it presents the advantage of a minimal equipment, easy handling, scalable to large surface areas, and has showed a high-quality performance as catalysts in photodegradation processes, that can be improved under the finding of optimal deposition conditions [17].

The efficiency of the photodegradation process of contaminants using semiconductor oxides as catalysts depends on several parameters, such as adequate crystal structure, surface morphology, and chemical composition, and large effective surface area, which in turn are defined by the deposition conditions, such as solution composition, annealing temperature and film thickness [18]. A detailed study of the effect of solution conditions can be crucial for manufacturing stable and efficient catalysts by low-cost processing. TiO_2 MB decoloration performance prevails over all others oxide semiconductors due to its chemical stability against photo corrosion under UV radiation, as occurs with other catalysts, as is the case of ZnO and SnO_2. This has stimulated different alternatives away to TiO_2. Suggested processing to enhance stability of ZnO and SnO_2, consider addition of dopants, composite formation, band gap engineering, and novel heterostructures [19].

It is important to highlight that there is a scarcity of reports comparing the decoloration efficacy of various semiconductor oxides, including TiO_2, ZnO, and SnO_2, which have been deposited using a consistent and cost-effective method under identical temperature conditions. Research on the degradation of methylene blue (MB) utilizing these three semiconductors in thin film form, all produced under the same cost-effective sol-gel technique while varying the film thickness, is limited. Additionally, low-cost techniques are known for their energy efficiency when compared to more expensive vacuum-based methods. It is generally anticipated that TiO_2 will consistently outperform the others, regardless of the deposition method used. This study evaluates the photocatalytic performance of SnO_2, ZnO, and TiO_2 in thin film configurations, deposited via the sol-gel technique, focusing on the decoloration of MB dye through both adsorption and degradation under UV light, with an emphasis on how film thickness influences these processes. Our objective was to identify the most effective oxide for maximizing MB degradation efficiency and to understand how the type of semiconductor oxide, its thickness, and physical characteristics impact the degradation of MB under controlled laboratory conditions that prioritize low energy consumption.

2. Experimental Procedure

 doi:10.20944/preprints202409.0880.v1

2.1. Deposition by Immersion or Dip-Coating Method

The film deposition was carried out using the immersion or dip-coating method. One of the advantages of this technique is that it allows the use of various precursor solutions and is highly versatile for different types of substrates, making it adaptable to diverse processes and substrate sizes. Additionally, it is relatively easy to operate and cost-effective. The stages of dip-coating deposition were as follows:

Immersion: The substrate is dipped into a container containing the precursor solution. This process must be carried out at a controlled speed to achieve uniformity in the deposited film.

Dwell time: The substrate remains immersed in the solution for a certain period, where the interaction between the solution and the substrate occurs.

Extraction: Similar to the immersion process, controlled extraction speed is required. As the substrate is pulled out of the solution, a layer of the precursor solution is carried out, resulting in the deposition of the film. Excess solution is drained from the surface. This stage is critical as extraction conditions greatly influence the quality of the film.

Evaporation: As the substrate is extracted from the solution, the solvent components such as H_2O and OH evaporate. The evaporation time of the solvent depends on its volatility and is affected by factors such as turbulence and variations in the atmosphere, such as relative humidity and dust, which can result in inhomogeneities throughout the film.

Final thermal treatment: The final stage involves subjecting the deposited film to a high-temperature drying process to remove residues and improve its physical properties [20–22]. Figure 1 shows the different stages of the dip-coating deposit process.

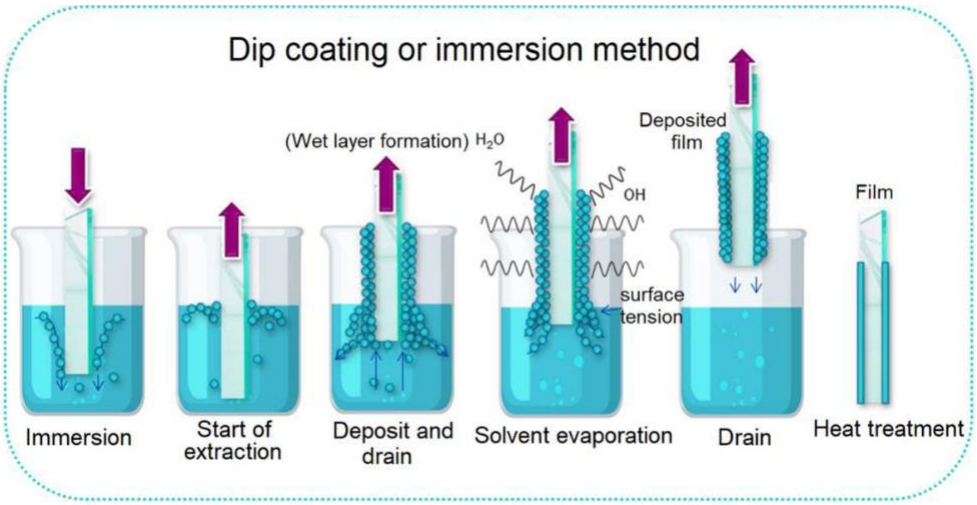

Figure 1. Diagram of the dip-coating method.

2.2. Samples Preparation

Prior to the film deposition process, the substrates underwent a cleaning process. In this study, soda-lime glass substrates (CORNING, 25 mm × 75 mm) were used as the substrate material. The cleaning process involved the following steps: the substrates were immersed in a 2 % dilute solution of Extran (MERCK), followed by rinsing with deionized water and then with ethyl alcohol (EtOH). The substrates were dried using a flow of nitrogen gas (INFRA, industrial line) and finally heated in an oven at 150 °C for 5 minutes to remove any residual moisture. The preparation method for the different films is described below. ZnO thin films were deposited from a 0.6 M solution prepared as follows: 16.4 g of zinc acetate ($Zn(CH_3COO)_2 \bullet 2H_2O$, Sigma Aldrich, United State) were dissolved in a mix of monoethanolamine (MEA, $NH_2CH_2CH_2OH$, Sigma Aldrich, United State) and methoxyethanol ($CH_3OCH_2CH_2OH$, Sigma Aldrich, United State), stirred in darkness a period of one hour. SnO_2 thin films were deposited from a 0.11 M solution prepared in the following way: 8.24 g of tin(II) acetate ($Sn(CH_3CO_2)_2$, Sigma Aldrich, United State) were dissolved in a mix of

 doi:10.20944/preprints202409.0880.v1

monoethanolamine (MEA) and methoxyethanol, stirred in darkness a period of one hour. TiO_2 thin films were deposited from a 0.17 M solution: 15 ml of titanium (IV) butoxide ($Ti(OCH_2CH_2CH_2CH_3)_4$, Sigma Aldrich, United State) were dissolved in ethanol. A second solution with deionized water, ethanol and hydrochloric acid was added to the first solution. Total dissolution was obtained after stirring in darkness a period of one hour. Previously cleaned soda lime glass substrate was immersed and withdrawn into the corresponding solutions with a velocity of 7.12 and 1.43 mm/s, respectively. This process was carried out at room temperature. Further annealing treatment at 250 °C for 9 min of films for solvent removal was carried out.

In order to observe the thickness variation, different immersions or cycles were performed. For ZnO: 2, 6 and 10 cycles, for TiO_2: 4, 7and 11 cycles and for SnO_2: 6, 10 and 16 cycles. Finally, an annealing for 1 h at 450 °C was performed for all the films in order to guarantee a complete synthesis. The objective of a comparation of deposition of three catalyst under similar conditions, limits the upper annealing temperature in order to explore the performance of each material. This restriction is also based in the fact that cheap glass substrates start to soft at high temperature reported in this work, increasing the undesirable incorporation of alkaline elements into the semiconductor lattice affecting adversely the performance of the catalysts.

The samples were labeled as described in Table 1.

Table 1. Nomenclature used to identify the samples according to the number of cycles used in the deposit.

TiO2		ZnO		SnO2	
Sample	Cycles	Sample	Cycles	Sample	Cycles
T100	4	Z100	2	S100	6
T200	7	Z200	6	S200	10
T300	11	Z300	10	S300	16

2.3. Characterization

Film thickness measurements were performed measuring the steps made by chemical etching. For ZnO, TiO_2 and SnO_2 films, diluted solutions of 10 % HCl (37 %), 5 % HF and HCl (37 %) with zinc powder were used, respectively. Film thickness measurements were conducted using a Dektak XT BRUKER profilometer with a vertical resolution of 0.1 nm, and compared with micrographs obtained with SEM. The structural properties of thin films were investigated by X-ray diffraction (XRD) PANalytical X'Pert PRO 45 device using Cu-Kα1 (λ = 1.5418 Å) radiation, Bragg-Brentano (BB) mode with an angle ranging between 20 and 80°. The surface morphology was analyzed by SEM JEOL JSM-5900LV, with an accelerating voltage of 1 kV, magnification = 80 KX, aperture size = 20 μm, and WD = 3.6 mm. The samples did not undergo any additional process to obtain the image of their surface. The photocatalytic activities of the films were made by the degradation of MB (Tetramethyl thionine chloride, $C_{16}H_{18}ClN_3S \bullet xH_2O$, Merck KGaA, Naucalpan, México), with a concentration of 1×10^{-5} M (pH ~ 9) dissolved in deionized water. 3 mL of 1×10−5 M (MB), was taken in a quartz cell (Hellma Analytics brand, 10 × 10 × 40 mm containing 3 mL of the MB solution), and a slice of film (10 × 9 mm^2) was immersed. A total 6 cells were irradiated with a 15.0 W Phillips germicide lamp G15T8 inside a cylindrical reactor. The distance between the film and the UV lamp was fixed to 3 cm. The optical absorbance in the range of 400 to 900 nm, was continuously monitored with an UV–vis spectrophotometer Shimadzu brand model 2400PC at intervals of 30 min for 150 min. The residual concentration of MB was calculated at a wavelength of 667 nm, which corresponds to the maximum intensity of MB absorption.

3. Results and Discussions

3.1. Structural Properties

Figures 2 shown the X-ray diffraction spectra of ZnO, SnO2, and TiO2 films obtained by dip coating. The spectra of SnO_2 and ZnO show the presence of definite diffraction peaks, indicating the

 doi:10.20944/preprints202409.0880.v1

polycrystalline character of the films, as shown in Figures 2a and 2b, respectively. On the other hand, the TiO_2 samples manufactured up to 450 °C do not exhibit any diffraction peaks. indicating the amorphous character of typical anatase phase. It is a matter of fact that some oxides change from amorphous to crystalline character beyond a critical temperature. This also applies to titanium dioxide, where annealing temperature up to 500 °C is the optimum condition for manufacturing quality catalyst for decoloration MB process. However, in the Photocatalisys Section it will be noted that no guarantee of better performance is assured in this annealing range. The X-ray spectrum of TiO_2 is shown in Figure 2c. In all X-ray diffraction spectra, a broad hump at 22.5 ° appears, indicating that all deposited films are thin in thickness, revealing the amorphous structure of the glass [23–25]. Only a wide signal appears showing the anatase phase. The diffraction peaks observed in SnO_2 and ZnO samples are consistent with those listed in the Joint Committee on Powder Diffraction Standards (JCPDS) card no. 41-1445 for rutile tetragonal type SnO2 structure [26] and 36–1451 for wurtzite type ZnO structure [27]. ZnO films present a preferential peak in the crystallographic direction (002), Figure 2 in comparison to the preferential peak in the plane (110) for SnO_2 films, Figure 3. Relatively ZnO films have a higher crystalline quality resulting in higher reflection of (002) planes. A much-detailed analysis about structural properties for SnO_2 and ZnO films as follows.

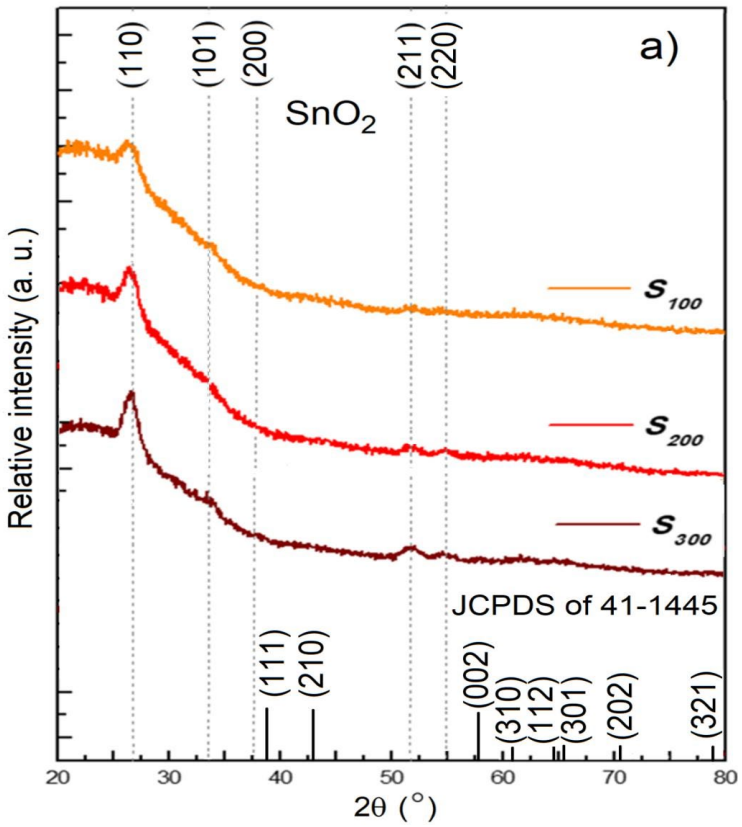

Figure 2. a. X-ray diffraction spectrum of SnO_2 films with different thickness and subjected to a heat treatment at 450 °C for 1 h.

 doi:10.20944/preprints202409.0880.v1

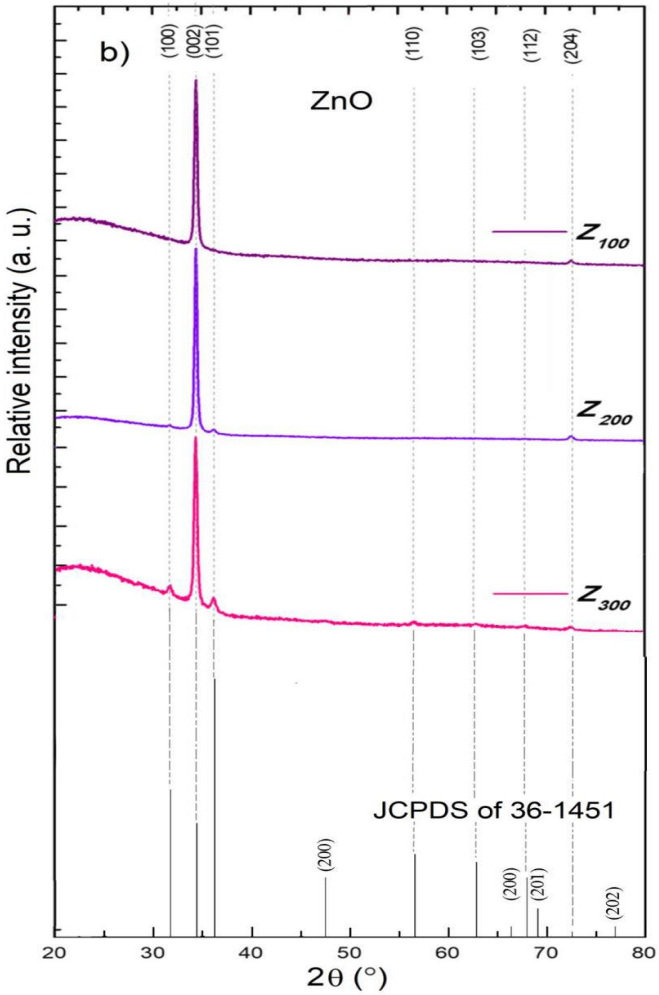

Figure 2. b. X-ray diffraction spectrum of ZnO films with different thickness and subjected to a heat treatment at 450 °C for 1 h.

Preprints.org (www.preprints.org) | NOT PEER-REVIEWED | Posted: 11 September 2024 doi:10.20944/preprints202409.0880.v1

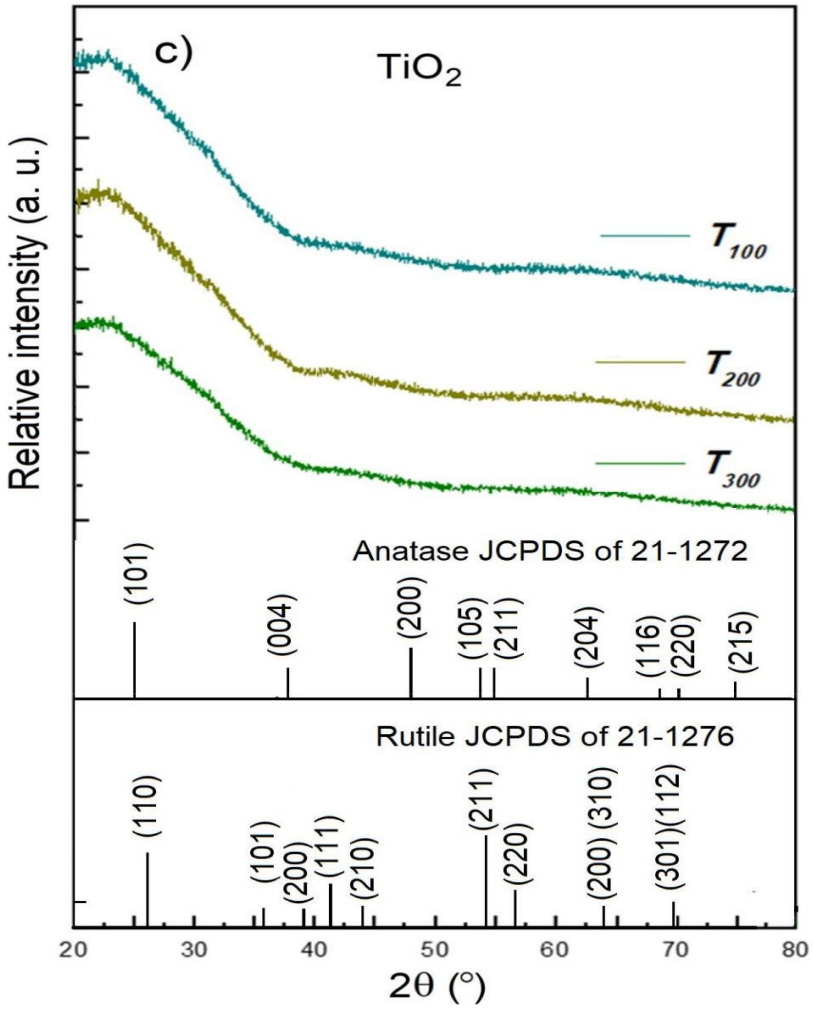

Figure 2. c. X-ray diffraction spectrum of TiO_2 films with different thickness and subjected to a heat treatment at 450 °C for 1 h.

The lattice parameters were obtained using the following way. From Bragg's law we obtain the interplanar distance d, equation 1.

$$2d \sin\theta = n\lambda \quad (1)$$

where λ is the wavelength of the X-rays (CuKα λ = 1.5418 Å) and n is an integer representing the diffraction order, in our case 1. The crystal size, D, is calculated using the Scherrer equation, equation 2 [28].

$$D = \frac{0.9\,\lambda}{\beta cos\theta} \quad (2)$$

where θ is the diffraction peak angle, β is the peak width at mean height (FWHM). The lattice constants c and a were obtained for the case of the SnO_2 film with tetragonal rutile phase, a = b, and (110) and (211) planes, according to the equations (3) and (4).

$$d_{hkl} = \frac{\lambda}{2\sin\theta_{hkl}} \quad (3)$$

$$\frac{1}{d_{hkl}} = \sqrt{\frac{k^2 + k^2}{a^2} + \frac{l^2}{c^2}} \quad (4)$$

 doi:10.20944/preprints202409.0880.v1

and in the case of the ZnO, hexagonal wurtzite phase, (002) and (101) planes were used, according to the Equations (5).

$$\frac{1}{d_{hkl}} = \sqrt{\frac{4(h^2 + hk + k^2)}{3a^2} + \frac{l^2}{c^2}} \quad (5)$$

The lattice constants a and c of bulk SnO_2 and ZnO are reported as a = 4.737 Å and c = 3.186 Å, and a = 3.25 Å and c = 5.20 Å, respectively [29]. Table 2 presents the values of the lattice constants c and a for SnO_2 and ZnO samples at different film thicknesses. TiO_2 films are amorphous, therefore their lattice constants could not be obtained. From the results obtained, it can be observed that as the film thickness increases (or as the number of cycles increases), the lattice constants of the films deviate from their bulk values, the c lattice constant decreases (the height of the basic cell decreases) and the a lattice constant increases (the basic cell widens).

Table 2. Calculated lattice constants, a and c and average crystallite size, D for SnO2 and ZnO films deposited with different film thickness.

Sample	D (nm)	a (Å)	c (Å)
S100	11	4.7842	3.1569
S200	11	4.8012	3.1329
S300	11	4.8165	3.0718
T100	35	----	5.2164
T200	35	3.2511	5.1984
T300	45	3.2636	5.1967

The dislocation density, δ, was calculated using the inverse square of the crystal size, D, equation 6 [30].

$$\delta = \frac{1}{D^2} \quad (6)$$

Also the TC texture coefficient was obtained using equation 7 [31].

$$T_C = \frac{\frac{I(hkl)}{I_0(hkl)}}{N^{-1}\sum_n \frac{I(hkl)}{I_0(hkl)}} \times 100\% \quad (7)$$

where I(hkl) and I_0(hkl) are the relative intensity of the plane and the standard intensity of the peak, respectively. The values of I_0(hkl) were taken from the standard, JCPDS, and N is the total number of peaks present in the X-ray spectrum. The preferred orientation of the peaks were (002) and (110) for SnO_2 and ZnO films, respectively. The density of dislocations and texture coefficients are presented in Table 3. It can be observed that as the thickness increases, the crystalline quality improves for both films, as the density of dislocations decreases and the number of crystal planes oriented towards the preferred direction increases.

Table 3. Dislocation density and texture coefficient of the SnO_2 and ZnO films deposited at different ratio of film thickness.

Sample	δ (×10⁷)	TC(002)
S100	9.09	1.875
S200	9.09	1.97
S300	8.33	2.06
		TC(110)
Z100	2.85	1.29
Z200	2.85	3.03
Z300	2.22	3.7

 doi:10.20944/preprints202409.0880.v1

3.2. Raman Analysis

As XRD analysis does not confirm positively the presence of TiO_2, then samples were studied by Raman spectroscopy in order to confirm the formation of TiO_2 in the obtained films. Irrespective of crystalline or amorphous phase, Raman spectroscopy can be utilized to observe the presence of material due to the Raman vibrational modes. Typical Raman spectra of TiO_2 anatase phase possess six different modes, where three of them are of Eg mode at 142, 200 and 654 cm^{-1}, one B_{1g} mode at 397 cm^{-1} and one A_{1g} +B_{1g} mode at 522 cm^{-1} [32]. Raman spectra of TiO_2 thin films obtained in this work is shown in Figure 3 (with a thickness of 227 nm) and is in good agreement with the reported Raman modes of TiO_2 anatase phase [33]. All the peaks were moderately sharp and intense which can be considered as the proof of a non-long-range order of the thin films.

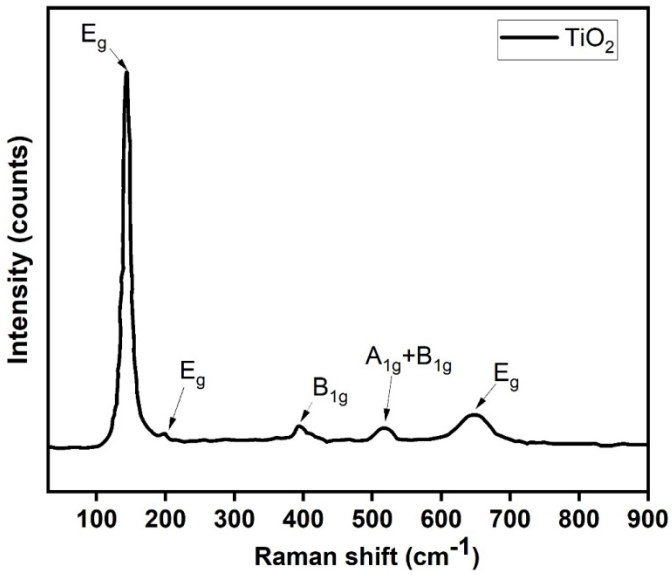

Figure 3. Raman spectra for TiO_2.

3.3. Morphological Properties for SnO_2, ZnO and TiO_2 Films

Figures 4 show the surface morphology of SnO_2, ZnO, and TiO_2 films. In general, all the deposited thin films exhibit a porous surface with nanometric spherical and irregular-shaped morphology. It can be observed that the morphological properties of semiconductor oxides are not greatly influenced by the film thickness, unlike the case of ZnO films, where with greater thickness, there is a larger grain size. The average grain size mentioned was directly measured using a ruler on a group of representative grains. In the case of SnO_2 films, no notable changes in the grain size and shape were observed (Figures 4a-c, the average grain size for all films is 11 nm). For ZnO films, it can be observed that the grain size increases with the film thickness. It is also important to mention that the rate of increase in the grain size is not gradual with respect to the thickness, but rather it increases abruptly (Figure 4d-f, the grain size changes from 11 nm for films with a thickness of 100 nm to 30 nm for a film thickness of 200 and 300 nm). Although the growth of the grains occurs through the coalescence of small grains. For the TiO_2 films, it is observed that the grain size is also small (Figures 4g-i, the grain size is 10 nm for all films). It should be noted that for thin thicknesses, no grain growth was observed in some areas of the film surface (Figure 4g).

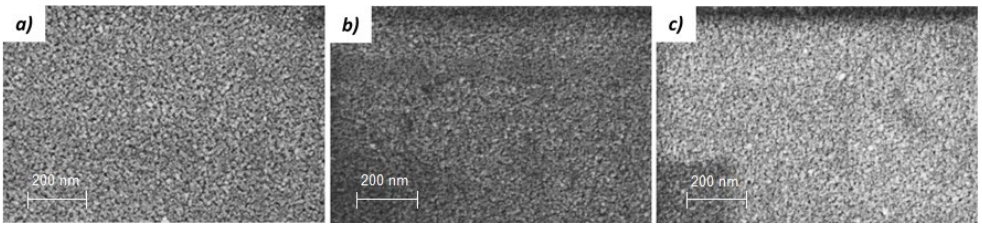

 doi:10.20944/preprints202409.0880.v1

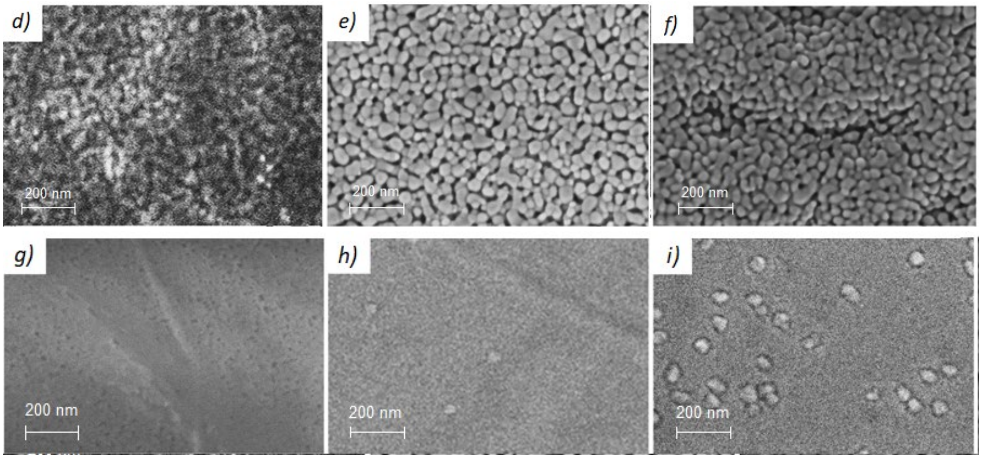

Figure 4. SEM micrographs of SnO_2 films (a-c), ZnO films (d-f), TiO_2 films (g-i).

3.4. Measurement of Thickness for SnO_2, ZnO, and TiO_2 Films

The thickness of some SnO_2, ZnO, and TiO_2 films were obtained using cross sectional view by scanning electron microscopy technique, and the images are shown in Figure 5. The images were captured transversely to the film and in some films were not possible to observe the film/substrate interface, due to the difficulty in cutting the samples without damaging the film. In general, the measurements obtained are very close to the expected thicknesses.

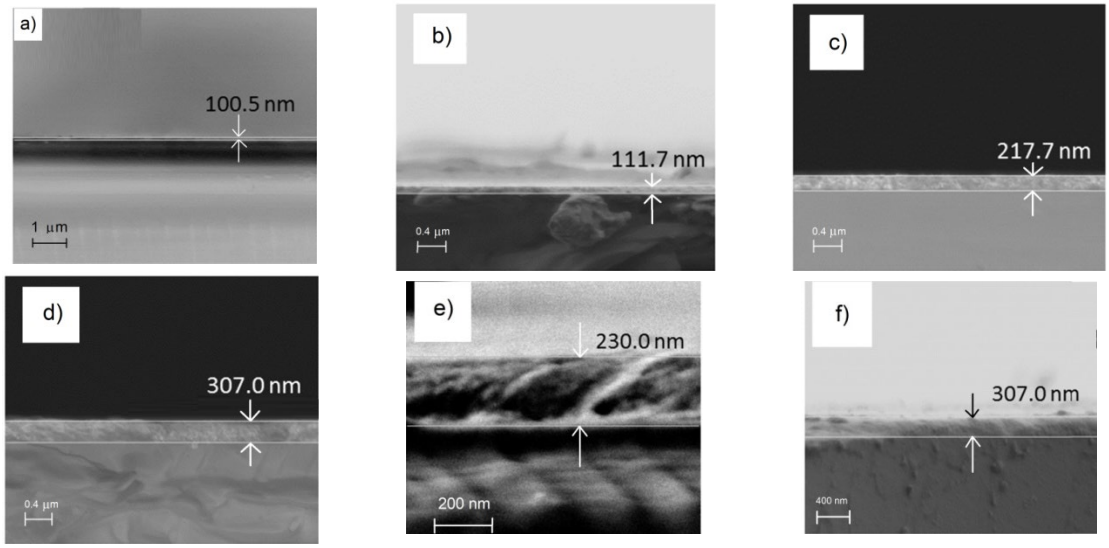

Figure 5. Cross-sectional SEM images for SnO_2, with 4 cycles (a), ZnO with 2, 6 and 10 cycles (b, c and d) and TiO_2 with 10 and 16 cycles (e, and f).

Thickness measurements were also obtained from profilometry, where the thicknesses are averaged from measurements taken at three different positions on the fabricated step. Table 4 presents the results obtained from both measurement techniques, and it can be observed that the film growth is nearly linear with respect to the number of immersions. Each film has a different growth rate, therefore different numbers of immersions were performed for each film to achieve thicknesses close to 100, 200, and 300 nm, as mentioned in the experimental development section. The results of the film thickness obtained by both measurement techniques are similar, except for the films with the smallest thicknesses (100 nm), where it is more difficult to measure with profilometry. The obtaining of thicknesses by profilometry technique is more economical compared to the SEM technique, and it is also reliable. As we mentioned in the previous section 3.3, the morphology of the films resulted in very small grains around 11 nm for SnO_2 and TiO_2 films and 30 nm for ZnO films, therefore obtaining RMS roughness values is difficult for SnO_2 and TiO_2 films. Below, we present grain size and RMS

 doi:10.20944/preprints202409.0880.v1

roughness values obtained by SEM and film thickness values by profilometry technique. It is observed that the RMS roughness increases as the film thickness increases, this is because the average height of the grains was taken as the film thickness, therefore, as the height of the grains increases, the surface roughness increases and consequently increases the effective surface area of the films.

Table 4. Film thicknesses, grain size and RMS roughness obtained on SnO_2, ZnO and TiO_2 films with different film thickness.

	TiO_2			ZnO			SnO_2		
Measurement technique	**T100**	**T200**	**T300**	**Z100**	**Z200**	**Z300**	**S100**	**S200**	**S300**
Film thickness by SEM (nm)	100.5	----	----	----	217.7	307	----	230	307
Film thickness by AFM (nm)	51	153	227	125	195	296	125	185	304
Average grain size by SEM (nm)	11	13	12	11	30	30	12	11	11
RMS roughness by SEM(nm)	19.63	29.21	41.65	20.82	43.19	64.09	8.42	20.17	33.57

The histograms of the RMS roughness values were obtained from SEM images through image processing, considering that the grain height was obtained from the film thickness. These histograms for all films are presented in Figure 6. It can be observed that for SnO_2 and ZnO films, the distribution in grain height changes from having on average shorter grains at lower and medium thicknesses (100 – 200 nm) to a distribution of taller grains for larger thicknesses (300 nm), this is better observed for ZnO films. We can say that, on average, having more grains with greater height increases the effective area of the films. For TiO_2 films, the distribution in grain height hardly changes with respect to the film thickness; that is, most of the grain height remains at half of the maximum film thickness.

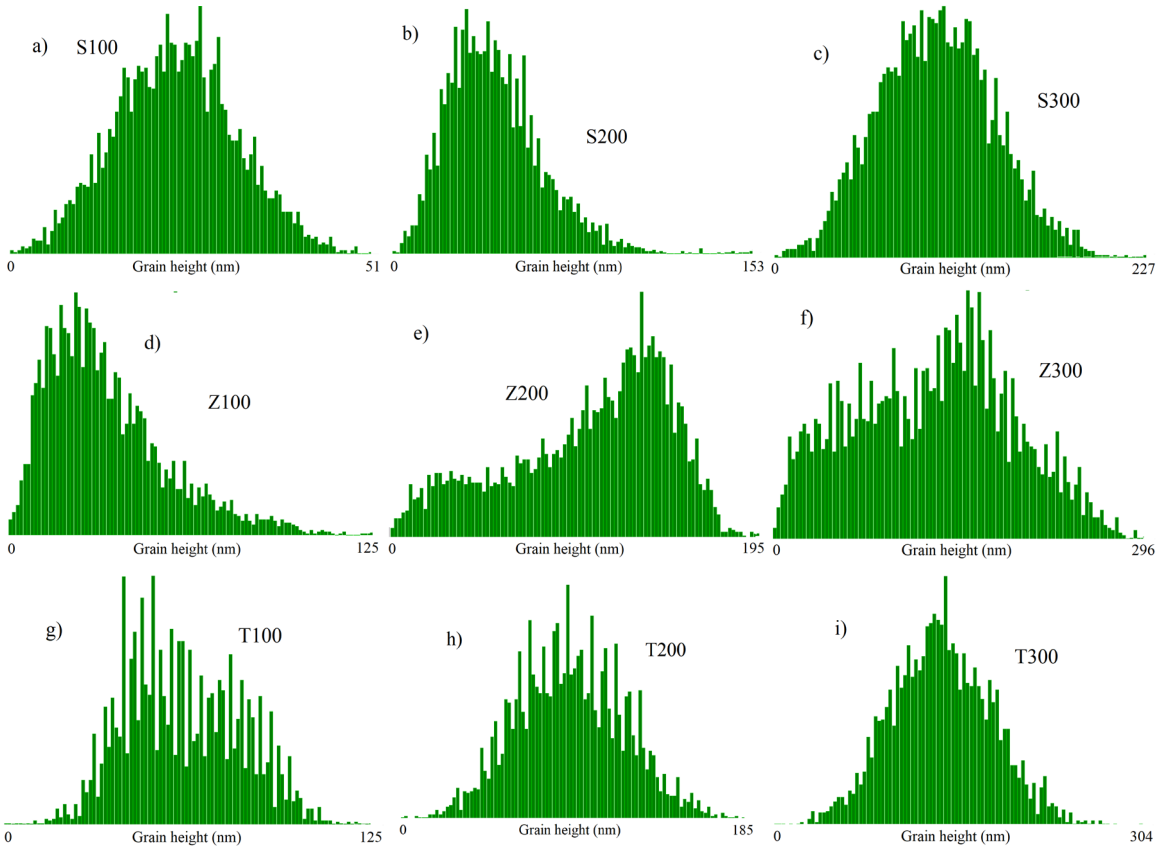

 doi:10.20944/preprints202409.0880.v1

Figure 6. Histogram of RMS roughness obtained from SEM and profilometry for all films.

3.5. Photocatalysis Study

The efficiency of decolorization or degradation (FD%) is determined by the difference in MB concentrations in darkness and under ultraviolet illumination at any given time, $\boldsymbol{C_0}$ and $\boldsymbol{C_t}$, respectively, according to the following equation 8.

$$FD\% = \frac{C_0 - C_t}{C_0} \text{x } 100 \quad (8)$$

It can be assumed that the concentrations of the dye, $\boldsymbol{C_0}$, $\boldsymbol{C_t}$ and the optical absorptions, $\boldsymbol{A_0}$, $\boldsymbol{A_t}$ are directly proportional, therefore equation 9 can be written as follows:

$$FD\% = \frac{A_0 - A_t}{A_0} \text{x } 100 \quad (9)$$

where $\boldsymbol{A_0}$ and $\boldsymbol{A_t}$ are the values of the optical absorbance of MB in darkness and under UV illumination at a given time, t, respectively. To obtain the optical absorption spectra, first a calibration curve is generated using a cell without MB content, and then the absorption spectra are obtained for each film introduced in a solution containing MB at established time intervals. The percentage of photocatalytic degradation of MB is determined from the absorption spectra by measuring the relative magnitude of the peak height of maximum absorption of MB, in our case, this occurred at a wavelength of 664 nm. We present the absorption spectra for all samples, showing the percentage of MB degradation, Figure 7.

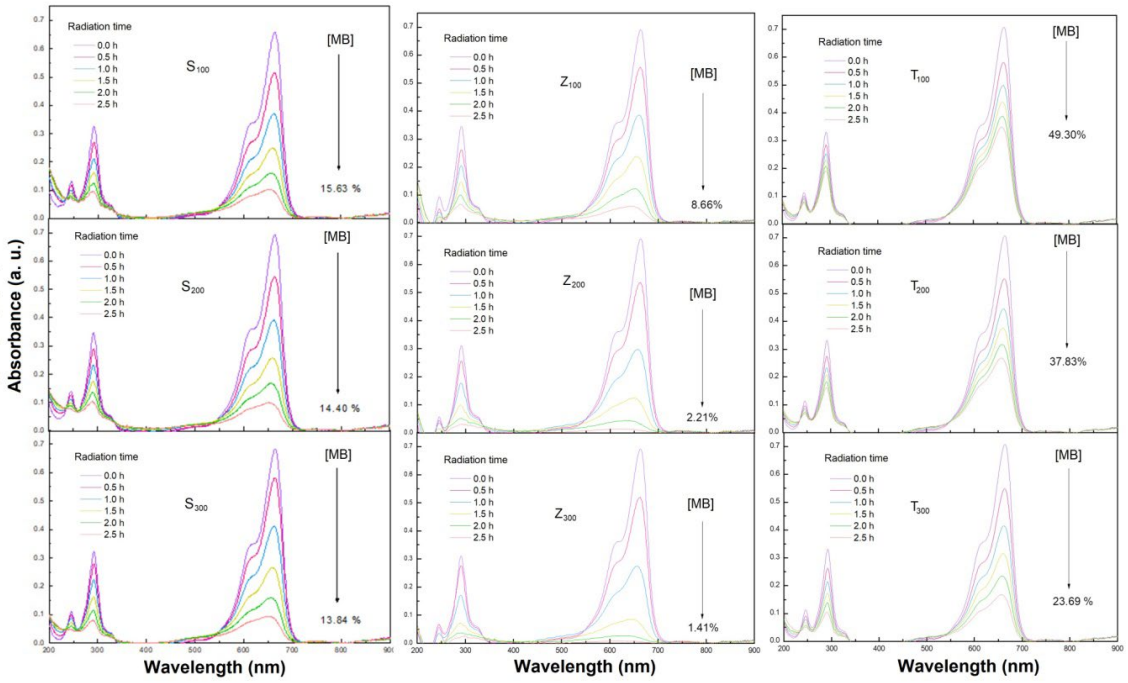

Figure 7. AM degradation curve in the photocatalysis process, sample Z300.

In Figure 8, the degradation performance of MB is shown for every 30 minutes of UV light exposure for all films deposited with different materials and thicknesses. All the films exhibit similar behavior; however, they show different degrees of degradation when exposed for different times. It is clearly observed that ZnO films are the most effective in degrading MB, reaching almost 100 %, followed by SnO_2 samples with a degradation percentage of 84 - 86 %, and finally, TiO_2 films are the least effective in degrading MB, with 50 – 76 % degradation.

Preprints.org (www.preprints.org) | NOT PEER-REVIEWED | Posted: 11 September 2024 doi:10.20944/preprints202409.0880.v1

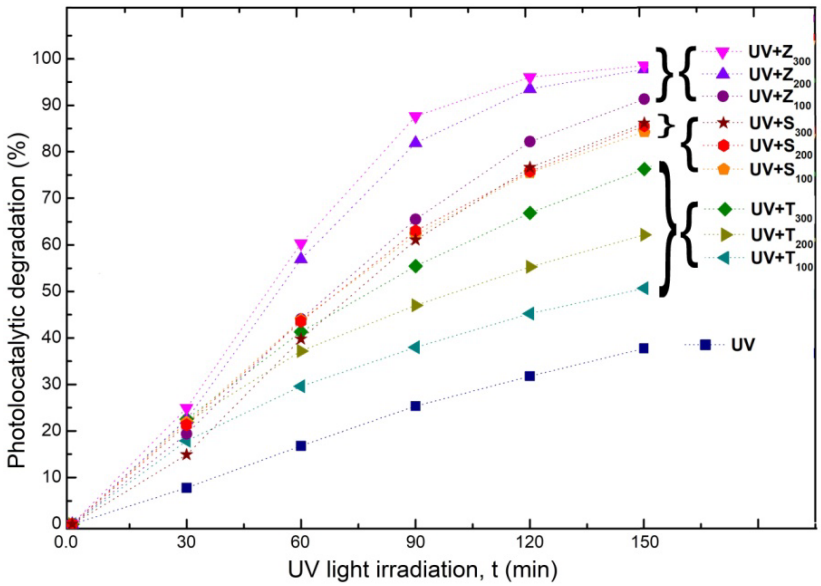

Figure 8. Films exhibit enhanced degradation of MB through the photocatalytic process as the UV light exposure time increases, varying material and thickness.

To determine the degradation kinetics of the dye and obtain the degradation or reaction rate constant, k (h-1), the Langmuir-Hinshelwood model was used, as the degradation rate of these organic compounds at low dye concentrations follows pseudo-first-order kinetic model [34], equation 10.

$$\ln\left(\frac{C_0}{C_t}\right) = kt \qquad (10)$$

Similar to the degradation percentage FD%, equation 11, the dye concentrations, $\mathbf{C_0}$ and $\mathbf{C_t}$, can be substituted with optical absorbance, $\boldsymbol{A_0}$ and $\boldsymbol{A_t}$, respectively, resulting in the following equation [35].

$$ln\left(\frac{A_0}{A_t}\right) = kt \qquad (11)$$

Plotting $\ln(A_o/A_t)$ with irradiation time, t, the slope of this line corresponds to the reaction rate constant, k, according to equation 11. Figure 9 shows the reaction rate constants, k, for the 9 deposited samples. Plotting the values of k for each sample, it can be observed that, similar to Figure 6, the most efficient samples for degrading MB are the ZnO films, followed by the SnO_2 samples, and the least efficient samples are the TiO_2 films. The next section provides an explanation of the behavior of the reaction rates.

Preprints.org (www.preprints.org) | NOT PEER-REVIEWED | Posted: 11 September 2024 doi:10.20944/preprints202409.0880.v1

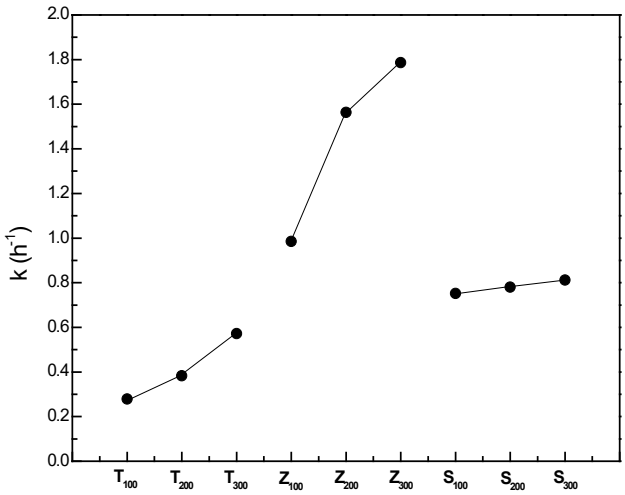

Figure 9. Reaction rate values, k, for the different films deposited with different film thicknesses.

The values of photocatalytic degradation and reaction rate for all deposited films are presented in Table 5. It can be observed in general that both photocatalytic degradation and reaction rate increase as the film thickness increases. ZnO films show the highest response due to their better physical properties.

Table 5. Degradacion fotocatalitica y razón de reacciones para todas las películas de ZnO depositadas.

Film	Photocatalytic degradation (%)	K (h^{-1})
S100	84.3	0.75
S200	85.6	0.79
S300	86.1	0.81
Z100	91.3	0.96
Z200	97.7	1.53
Z300	98.6	1.79
T100	50.7	0.27
T200	62.1	0.38
T300	76.3	0.58

In Table 6, we are comparing our obtained results with others reported for the degradation efficiency of MB, for the three semiconductor oxides used in this work, under somewhat similar measurement conditions. It can be observed that our results presented in this work are competitive with other findings.

Table 6. Comparison of our magnitudes of MB degradation obtained with others reported in the scientific literature.

Material	Degradation (%)	UV irradiation time (min)	MB concentration	Reference
SnO_2	60	120	0.1 mg/L	[36]
SnO_2	90	120	10 mg/L	[37]
ZnO	99	100	20 ppm	[38]
ZnO	99	180	50 mg/L	[39]
TiO_2	50	105	250 ppm	[40]

 doi:10.20944/preprints202409.0880.v1

TiO_2	95.2	240	10 ppm	[41]
SnO_2	87	120	10 mg/L	Our result
ZnO	98	120	10 mg/L	Our result
TiO_2	76	120	10 mg/L	Our result

4. Mechanism of Photodegradation

The degradation of MB dissolved in water is carried out through heterogeneous photocatalysis using semiconductor oxides as catalysts. The general mechanism of the photocatalytic process consists of several stages, which are described as follows [42]:

Generation of electron-hole pairs: This step occurs when light with photons whose energy is equal to or greater than the bandgap of the semiconductor oxide ($h\nu \geq E_G$) is incidenced on it. These photons are absorbed by the semiconductor oxide, exciting electrons in the conduction band e_{bc}^- and leaving holes in the valence band h_{bv}^+, thus generating electron-hole pairs:

$$semiconductor\ oxide + h\nu \longrightarrow e_{cb}^- + h_{vb}^+ \quad (12)$$

Formation of reactive species: The generated electron-hole pairs migrate by diffusion to the surface of the semiconductor, leading to redox processes by charge transfer with absorbed species on the surface, in this case, molecules of the MB dye in water. The holes h_{vb}^+ react with water H_2O or hydroxide ions OH^- to produce ionized species:

$$(H_2O\ or\ OH^-) + h_{vb}^+ \longrightarrow \bullet OH \quad (13)$$

Meanwhile, the electrons e_{cb}^- are captured by adsorbed oxygen molecules (O_2) to produce the superoxide radical anion:

$$(O_2)_{ads} + e_{CB}^- \longrightarrow O_2^{\bullet -} \quad (14)$$

Degradation of the dye: Both •OH and $\mathbf{O_2^{\bullet -}}$ react with the organic molecules of the MB dye in the aqueous medium, leading to its degradation, production of degradation intermediates, as described in equations 15 and 16.

$$\bullet OH + MB \longrightarrow intermediate\ products \longrightarrow H_2O + CO_2 + mineral\ acids \quad (15)$$

$$O_2^{\bullet -} + MB \longrightarrow intermediate\ products^* \longrightarrow H_2O + CO_2 + mineral\ acids \quad (16)$$

Degradation products: During the dye degradation process, different intermediate products can be formed depending on various factors such as the catalyst used, pH of the medium, and other species or molecules present in the aqueous medium. In this stage, the conversion to less harmful molecules, mainly H_2O, CO_2 as well as minerals acids or inorganic acids containing hydrochloric, sulfuric and nitric acids among others. Almost all the elements that make up the organic contaminant, i.e., carbon, nitrogen, and sulfur, are converted into non-polluting organic species. This is due to the properties of the most important degrading species in the process, the •OH radical. After the formation of final products, they are distributed in the aqueous medium through diffusion. From the above, it can be said that to achieve higher efficiency in MB degradation, it is required to have: 1) Higher production of electron-hole pairs, which can be achieved by doping the semiconductor oxide with donor or acceptor atoms, and 2) Longer lifetime of photogenerated electron-hole pairs in their respective bands, i.e., electrons in the conduction band and holes in the valence band. To prolong the lifetime of charge carriers in their respective bands, a semiconductor with good crystalline quality is required [43], as semiconductors with poor crystalline quality will contain more structural defects with energy levels near the center of the bandgap, which trap and retain charge carriers for longer, preventing them from reaching their respective bands, diffusing, and subsequently forming reactive species necessary for MB degradation [44,45] This is illustrated in Figure 10.

Preprints.org (www.preprints.org) | NOT PEER-REVIEWED | Posted: 11 September 2024 doi:10.20944/preprints202409.0880.v1

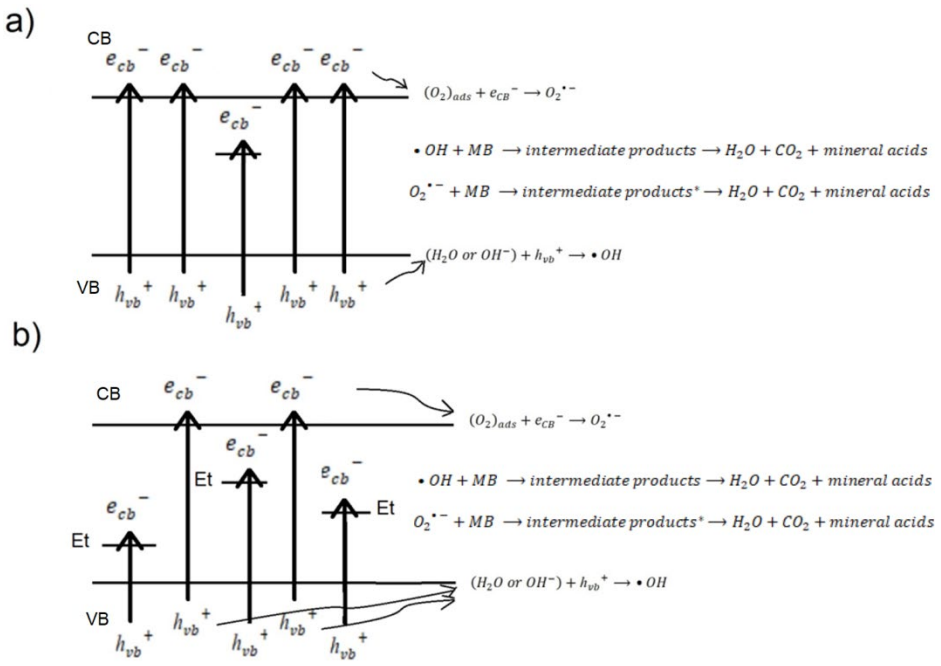

Figure 10. Shows semiconductor with different crystalline quality: (a) a semiconductor with good crystalline quality, containing few structural defects and few energy levels within the band gap, and (b) a semiconductor with poor crystalline quality, containing more structural defects and therefore more energy levels within the band gap. The conduction band (CB), valence band (VB) and trap energy level (Et) are also labeled.

Semiconductors with good crystalline quality have fewer defects and therefore fewer energy levels close to the center of the band gap. Additionally, having large grains on the film surface results in fewer dangling bonds. These two conditions allow more photo-generated charge carriers to reach their respective bands and participate in the photodegradation process, as fewer charge carriers are trapped and retained in structural defects. Comparing the physical properties of the three deposited films, it can be concluded that the films made of ZnO have the best structural properties. This is because their lattice constants are close to the volume values, they have larger crystal grain sizes (D), as shown in Table 2, and the majority of their crystal planes are oriented towards a preferred direction or a higher texture coefficient (TC), as shown in Table 3. The morphological properties of the ZnO films also consist of large grains, although they are formed by the coalescence of smaller grains, as seen in Figures 4 (e-f). Therefore, the ZnO films are the most efficient in the degradation of MB. On the other hand, the TiO_2 films are the least efficient in the degradation of MB, as they have the poorest structural properties, being even amorphous, with the smallest grain sizes compared to the other semiconductor oxide films. From our results, it can be concluded that having poor crystalline quality favors less grain growth and therefore more dangling bonds on the film surface.

In the literature, TiO_2 stands out as the most promising solution for addressing water contamination, thanks to its cost-effectiveness, lack of toxicity, and enduring stability. This semiconductor has direct or indirect forbidden energy bands. Zhang et al. [46] demonstrate that TiO_2 in its anatase phase has an indirect forbidden energy band, which means that the lifetime of photo-generated carriers is longer due to phonon-assisted recombination, promoting maximum efficiency in the photocatalytic evolution of MB. Electron mobility is higher in the case of the anatase phase due to its lower effective electron mass. ZnO is the second most studied semiconductor oxide for its application as a photocatalyst, similar to TiO_2. However, ZnO is very economical and environmentally friendly. This semiconductor oxide is usually synthesized in wurtzite hexagonal form. SnO_2 is another semiconductor oxide that combines high optical transmittance and electrical conductivity suitable for application as a photocatalyst; this semiconductor grows in rutile phase. SnO_2 has the highest forbidden band width value from 3.6 to 3.8 eV. These three semiconductor

Preprints.org (www.preprints.org) | NOT PEER-REVIEWED | Posted: 11 September 2024 doi:10.20944/preprints202409.0880.v1

oxides have large forbidden band widths above 3.2 eV, therefore, only the UV light range from solar radiation, corresponding to 3 % of the total sunlight, will be utilized. Another important parameter for dye degradation is the exciton binding energy, which indicates the time that electron-hole pairs last before recombining and thereby more efficiently affecting light-induced chemical reactions in a photocatalytic material. In this case, TiO_2, having the largest exciton binding energy value, is the most suitable for degrading a dye.

Although, as we have observed with the deposition conditions used in this study, the ZnO film exhibits the best physical properties, followed by SnO_2. In the case of TiO_2 its physical characteristics are not as good as we would like; in fact, this semiconductor turned out to be amorphous. In Table 7, we present some volume physical characteristics of the 3 semiconductor oxides analyzed in this study.

Table 7. Summary of SnO_2, ZnO and TiO_2 physical properties [54].

Film	Optical absorption edge: Eg (eV)	Excitonic binding energy (meV)	Crystal structure	Electronic band strycture
TiO_2	⊥ (direct) anatasa 3.420 Rutilo 3.035 ∥ (indirect) anatasa 3.460 Rutilo 3.051	Rutile 4 [47] Anatase 180 [48]	Anatase (tetragonal). Rutile (tetragonal) brookite (orthorhombic)	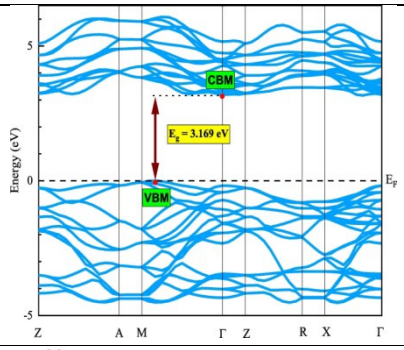 [51]
ZnO	3.370 – 3.437	60	Wurtzita hexagonal [49]	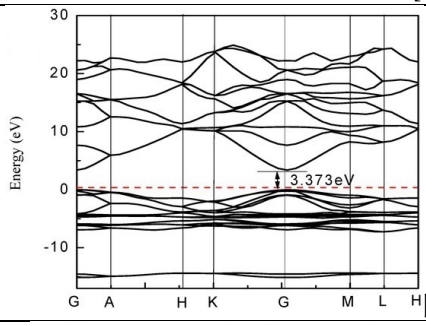 [52]
SnO_2	3.6 – 3.8	130	Cassiterite or rutile phase [50]	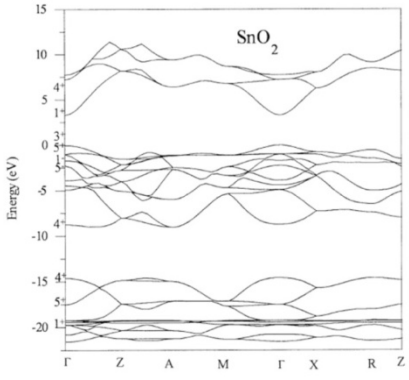 [53]

Starting from optical transmittance measurements and using equation 17 (Lambert-Beer's law), the absorbance value is obtained for some films and presented in Figure 11.

$$A = -Log(\frac{I}{I_o}) \quad (17)$$

 doi:10.20944/preprints202409.0880.v1

It is confirmed that all films have higher absorbance, which further enhances the photocatalytic process, the band gaps are 3.23, 3.25 and 3.24 for ZnO, SnO_2 and TiO_2 films, respectively.

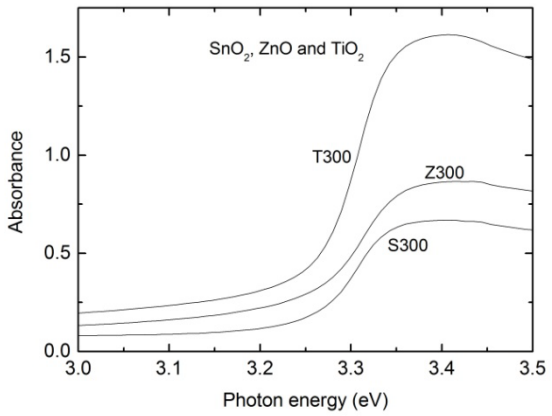

Figure 11. The absorbance for SnO_2, ZnO and TiO_2 films.

5. Reusability of the Photocatalyst

The recyclability of the catalyst in the ZnO film with a thickness close to 300 nm was analyzed, as this film showed the best degradation results for MB. The analysis was performed by repeating the MB decolorization process three times on the same film. Before each cycle, the film was subjected to heating at 200 °C for 1 hour to remove any residual products remaining on the film's surface after the reaction. The results are shown in Figure 12, indicating that the degradation efficiency of the ZnO film decreased to 97 % in cycle 2, 94 % in cycle 3, and finally, 92 % in cycle 4. It was found that the MB, in contact with the ZnO surface, caused wear or abrasion, resulting in a decrease in the film's thickness and the impregnation of a layer of MB at least 30 nm thick (which was removed with the heating process). Therefore, the decrease in film thickness is the cause of the decrease in MB degradation efficiency.

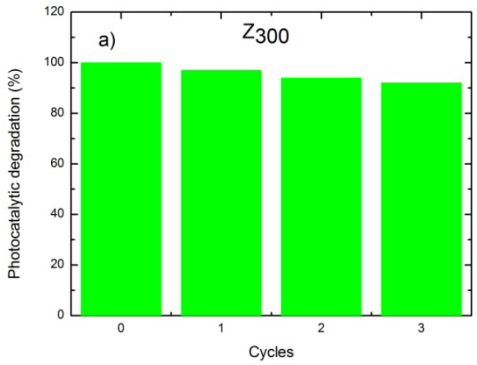

Figure 12. Percentage of MB degradation for ZnO films with a thickness of 300 nm and measurement conditions that provided the maximum MB degradation for 4 cycles.

6. Conclusions

Films of SnO_2, ZnO, and TiO_2 were successfully fabricated utilizing the dip coating technique and subsequently assessed for their photocatalytic potential. Specifically, the SnO_2 films displayed a rutile tetragonal structure, while the ZnO films exhibited a wurtzite crystalline structure. The preferred growth planes identified were the (110) and (002) planes for SnO_2 and ZnO, respectively. Among these, the ZnO films demonstrated superior structural attributes, as their lattice constants closely aligned with the volume values, the crystal grain size (D) was the largest, and they possessed a greater number of crystal planes oriented towards a specific crystallographic direction, resulting in

 doi:10.20944/preprints202409.0880.v1

a higher texture coefficient (TC) and a reduced density of dislocations (δ). Furthermore, the ZnO films presented larger grains in their surface morphology. Collectively, these characteristics contribute to a reduction in defects within both the volume and surface of the film, leading to fewer energy levels near the center of the band gap, which enhances the ability to trap and retain charge carriers for extended periods. The degradation of MB is contingent upon the generation rate of carriers and their longevity within their respective bands, thereby rendering the ZnO films the most effective for MB degradation. Raman spectroscopy was employed to verify the presence of TiO_2 material. A correlation was noted between the structural properties and surface morphology; specifically, films with high crystalline quality, such as the ZnO films, exhibited greater grain growth in a preferred crystallographic direction, whereas films with lower crystalline quality, like the TiO2 films, showed minimal or no grain growth. The efficiency of MB degradation diminishes with a decrease in film thickness, attributed to the lower structural quality of thinner films, and for reused films, this reduction is due to the degradation of the film caused by the dye.

Author Contributions Heberto Gomez performed writing and discussion, T. V. K. Karthik interpretation of results and M. de la L. Olvera and A. Maldonado review, support technique and editing.

Funding This research was funded by A. Maldonado credits CONACyT for support through 166601 Project and Programa de Desarrollo al Profesorado, PRODEP.

Data availability The data that supports the findings of this study are available in this article.

Acknowledgments The authors are thankful to Ing. Emma Luna-Arredondo, A. Tavira and M. A. Luna-Arias for the technical help rendered.

Declaration of competing interest The authors declare that there is no conflict of interest.

References

1. O'Neill, C.; Hawkes, F. R.; Hawkes, D. L.; Lourenço, N. D.; Pinheiro, H. M.; Delée, W. Colour in textile effluents - Sources, measurement, discharge consents and simulation: A review. *J. Chem. Technol. Biotechnol*. **1999**, *74*, 11, 1009–1018.
2. Bae, J. S.; Freeman, H. S.; Kim, S. D. Influences of new azo dyes to the aquatic ecosystem. *Fibers Polym*. **2006**, **7**, 1, 30–35.
3. Zhu, B.; Chen, W. F.; Koshy, P. Sorrell, C. C. Effect of film thickness on the phototcatalytic performance of TiO2 thin films deposited by spin coating. *Am. Ceram. Soc*. **2015**.
4. Garud R. M.; Kore S. V.; Kore V. S.; Kulkarni G. S. A Short Review on Process and Applications of Reverse Osmosis. Universal *Journal of Environmental Research and Technology*. **2011**. *1*, 3 233-238.
5. Sangwoo, S.; Orest, S.; Patrick, B. Warren, Howard A. Stone, Membraneless water filtration using CO_2, *Nature Communications* **2017**. *8*, 15181.
6. Gianluca, C.; Nicola, R.; The treatment and reuse of wastewater in the textile industry by means of ozonation and electroflocculation, *Water Research*, **2001**. *35*, 2, 567-572
7. Colmenares, J. C. Yi-Jun, X., Heterogeneous Photocatalysis From Fundamentals to Green Applications, Springer, *Green Chemistry and Sustainable Technology*. Doi 10.1007/978-3-662-48719-8.
8. Xueting,C.;Zhongliang, L.;Xinxin, Z.;Shibin, S.; Danxia, G.;Lihua, D.;Yansheng, Y.;Yanqiu Z.; Efficient synthesis of sunlight-driven ZnO-based heterogeneous photocatalysts, *Materials & Design*, **2016**, *98*, 324-332.
9. Alves do Nascimento, J. L.; Chantelle, L.; Garcia dos Santos, I. M.; Menezes de Oliveira, A. L. Ferreira Alves, M. C. The Influence of Synthesis Methods and Experimental Conditions on the Photocatalytic Properties of SnO_2: A Review. *Catalysts*. **2022**, *12*(4), 428; https://doi.org/10.3390/catal12040428.
10. Gbenga Peleyeju, M.; Viljoen, E.L. WO_3-based catalysts for photocatalytic and photoelectrocatalytic removal of organic pollutants from water – A review, *Journal of Water Process Engineering*. **2021**. *40*, 101930.
11. Serpone, N.; Emeline, A. V Semiconductor Photocatalysis — Past, Present, and Future Outlook, *J. Phys. Chem. Lett*. **2012**, *3*, *5*, 673–677.
12. Tao, Y.; Schwartz, S.; Wu, C.Y.; Mazyck, D.W. Development of a TiO_2/AC composite photocatalyst by dry impregnation for the treatment of methanol in humid airstreams, *Ind. Eng. Chem. Res*. **2005**. *44*, 7366–7372.
13. Prado, A.G.S.; Bolzon, L.B.; Pedroso, C.P.; Moura, A.O.; Costa, L.L. Nb2O5 as efficient and recyclable photocatalyst for indigo carmine degradation, *Appl. Catal. B Environ*. **2008**. *82*. 219–224.
14. Luiz F. K.; Pedrinia, L.C.; Escaliantea, L.V.A. Deposition of TiO_2 thin Films by Dip-Coating Technique from a Two-Phase Solution Method and Application to Photocatalysis, *Materials Research*. **2021**. *24*. e20210007, doi.org/10.1590/1980-5373-MR-2021-0007.

15. Ferhunde, A.; Orkun, G. The effect of spinning cycle on structural, optical, surface and photocatalytic properties of sol–gel derived ZnO films, *Journal of Sol-Gel Science and Technology*. **2021**. *100*. 299–309. doi.org/10.1007/s10971-021-05661-4.
16. Chin-Yi.; Jui-Chung, W.; Jing-Heng, C.; Shih-Hsin, M.; Kun-Huang, C.; Tzyy-Leng, H.; Chien-Yie, T.; Chi-Jung, C.; Chung-Kwei, L.; Jerry J. W. Photocatalyst ZnO-doped Bi2O3 powder prepared by spray pyrolysis, *Powder Technology*, **2015**. *272*, 316-321. doi.org/10.1016/j.powtec.2014.11.036.
17. Obregón, S.; Rdz, V. Photocatalytic TiO2 thin films and coatings prepared by sol–gel processing: a brief review, *Journal of Sol-Gel Science and Technology*. **2018**. *102*. https://link.springer.com/article/10.1007%2Fs10971-021-05628-5.
18. Farsi, B. Al.; Souier, T.M..; Marzouqi, F. Al.; Maashani, M. Al.; Bououdina, M. Widatallah, H.M.; Abri, M. Al. Structural and optical properties of visible active photocatalytic Al doped ZnO nanostructured thin films prepared by dip coating, *OpticalMaterials*. **2021**, *113*. 110868.
19. Shaham-Waldmann, N., Yaron, P. Away from TiO_2: A critical mini review on the developing of new Photocatalysts for degradation of contaminants in water, *Materials Science in Semiconductor Processing* **2016**. *42*. 72–80.doi.org/10.1016/j.mssp.2015.06.068.
20. C.J. Brinker, A.J. Hurd, "Fundamentals of sol-gel dip-coating", J. Phys. III France 4 (1994) 1231-1242.
21. C.J. Brinker, "Dip coating", "Chemical Solution Deposition of Functional Oxide Thin Films", T. Schneller et al. (eds.), DOI 10.1007/978-3-211-99311-8_10, Springer-Verlag Wien 2013.
22. Tang, X., & Yan, X. (2016). Dip-coating for fibrous materials: mechanism, methods and applications. Journal of Sol-Gel Science and Technology, 81(2), 378–404. doi:10.1007/s10971-016-4197-7.
23. Amakali, T., Daniel, L. S., Uahengo, V., Dzade, N. Y., & de Leeuw, N. H. (2020). Structural and Optical Properties of ZnO Thin Films Prepared by Molecular Precursor and Sol–Gel Methods. Crystals, 10(2), 132. doi:10.3390/cryst10020132.
24. Akgul, F. A., Gumus, C., Er, A. O., Farha, A. H., Akgul, G., Ufuktepe, Y., & Liu, Z. (2013). Structural and electronic properties of SnO2. Journal of Alloys and Compounds, 579, 50–56. doi:10.1016/j.jallcom.2013.05.057.
25. Venkatachalam, T., Sakthivel, K., Renugadevi, R., Narayanasamy, R., Rupa, P., Predeep, P., … Varma, M. K. R. (2011). Structural and Optical Properties of TiO[sub 2] Thin Films. doi:10.1063/1.3643673.
26. Joint Committee on Powder Diffraction Standards (JCPDS), *International Centre for Diffraction Data*. **1997**, Card No. 41-1445.
27. McMurdie, H.F.; Morris, M.; Evans, E.; Paretzkin, B.; Wong-Ng, W.; Ettlinger, L.; Hubbard, C. Standard X-ray diffraction powder patterns from the JCPDS research associateship. *Powder Diffr*. **1986**, *1*, 64–77.
28. Cullity, B.D.; Stock, S.R. Elements of X-ray Diffraction, 3rd ed.; *Prentice Hall*: Upper Saddle River, **2001**. NJ, USA.
29. Madelung, O.; Rössler, U.; Schulz, M. (Eds.) II-VI and I-VII Compounds; Semimagnetic Compounds. Landolt-Börnstein—Group III Condensed Matter (Numerical Data and Functional Relationships in Science and Technology), Volume 41B; *Springer*: Berlin/Heidelberg, **1999**. Germany.
30. Khan Z R, Zulfequar M and Khan M S, Optical and structural properties of thermally evaporated cadmium sulphide thin films on silicon (1 0 0) wafers, *Mater. Sci. Eng. B*. **2010**, *174*. 145–149.
31. Harris, G. Quantitative measurement of preferred orientation in rolled uranium bars, *Dublin Philosophy. Mag. J. Sci.***1952**. *43*, 336, 113–123.
32. Wiatrowski, A.; Mazur, M.; Obstarczyk, A.; Wojcieszak, D.; Kaczmarek, D.; Morgiel, J.; Gibson, D. Comparison of the Physicochemical Properties of TiO2 Thin Films Obtained by Magnetron Sputtering with Continuous and Pulsed Gas Flow, *Coatings*. **2018**, *8*, *11*, 412. doi.org/10.3390/coatings8110412.
33. Sekiya, T.; Ohta, S.; Kamei, S.; Hanakawa, M.; Kurita, S. Raman spectroscopy and phase transition of anatase TiO2 under high pressure, *Journal of Physics and Chemistry of Solids*. **2001**. *62*. 717-721.
34. Tanaka, K.; Capule, M.F.V.; Hisanaga, T. Effect of crystallinity of TiO2 on its photocatalytic action. *Chem. Phys. Lett*. **1991**. *187*. 73–76.
35. Chang, Y. C.; Chen, C. M.; Guo, J. Y. Fabrication of novel ZnO nanoporous films for efficient photocatalytic applications. *J. Photochem. Photobiol. A Chem*. **2018**. *356*. 340–346.
36. Adeyemi, J. O., & Onwudiwe, D. C. SnS2 and SnO2 Nanoparticles Obtained from Organotin(IV) Dithiocarbamate Complex and Their Photocatalytic Activities on Methylene Blue. *Materials*, 2020. 13(12), 2766. doi:10.3390/ma13122766.Viet, P. V., Thi, C. M., & Hieu, L. V. (2016). The High Photocatalytic Activity of SnO_2 Nanoparticles Synthesized by Hydrothermal Method. *Journal of Nanomaterials*, **2016**, 1–8. doi:10.1155/2016/423104.
37. Swetha, P., Jayachamarajapura, P. S., Jayden, S., Syed, F. A., Mufsir, K., Mohammad, R. H., Baji, S., Kiran, K. Photocatalytic Degradation of Methylene Blue and Metanil Yellow Dyes Using Green Synthesized Zinc Oxide (ZnO) Nanocrystals. *Crystals* **2022**, 12(1), 22; https://doi.org/10.3390/cryst12010022..
38. Albiss, B., & Abu-Dalo, M. Photocatalytic Degradation of Methylene Blue Using Zinc Oxide Nanorods Grown on Activated Carbon Fibers. *Sustainability*. **2021**. 13(9), 4729. doi:10.3390/su13094729

39. Isai1, k. A., Shrivastava, V. S. Photocatalytic degradation of methylene blue using ZnO and 2%Fe–ZnO semiconductor nanomaterials synthesized by sol–gel method: a comparative study. *N Applied Sciences.* **2019**. *1:1247* https://doi.org/10.1007/s42452-019-1279-5.
40. Olga, T., Anastasia, M. M., Konstantinos, M. S., Ekaterini, P. Lakovos, Y. Highly Active under VIS Light M/TiO2 Photocatalysts Prepared by Single-Step Synthesis. *Appl. Sci.* **2023**, 13(11), 6858; https://doi.org/10.3390/app13116858.
41. Mohammad Jafri, N. N., Jaafar, J., Alias, N. H., Samitsu, S., Aziz, F., Wan Salleh, W. N., … Isloor, A. M. (2021). Synthesis and Characterization of Titanium Dioxide Hollow Nanofiber for Photocatalytic Degradation of Methylene Blue Dye. *Membranes*, 11(8), 581. doi:10.3390/membranes11080581.
42. Maness, P. C.; Smolinski, S.; Blake, D. M.; Huang, Z.; Wolfrum, E. J.; Jacoby, W. A. Bactericidal Activity of Photocatalytic TiO2 Reaction: toward an Understanding of Its Killing Mechanism. *Columbia: Applied and Environmental Microbiology*. **1999**. 4094–4098.
43. Landsberg, P.T. Recombination in semiconductors, *Cambridge,* **1991.**
44. Hunge, Y. M., Yadav, A. A., Kang, S. W., Mohite, B. M. Role of Nanotechnology in Photocatalysis Application, *Recent Patents on Nanotechnology*.**2023**.*17*, 1.10.2174/1872210516666220304162429.
45. Vasiljevic, Z. Z., Dojcinovic M. P.,Vujancevic, J. D. , Jankovic-Castvan. I., Ognjanovic, M., Tadic, N. B., Stojadinovic, S.,Brankovic, G. O., Nikolic, M. V. Photocatalytic degradation ofmethylene blue under natural sunlight using irontitanate nanoparticles prepared by a modifiedsol–gel method.*R. Soc. Open Sci*. **2020**. *7*: 200708.http://dx.doi.org/10.1098/rsos.200708.
46. J. Zhang, P. Zhou, J. Liu, J. Yu, Phys. Chem. Chem. Phys., 2014, 16, 20382-20386.
47. J. Pascual, J. Camassel, and H. Mathieu, "Fine structure in the intrinsic absorption edge of TiO2," Physical Review B, vol. 18, no. 10, pp. 5606–5614, 1978.
48. E. Baldini, L. Chiodo, A. Dominguez et al., "Strongly bound excitons in anatase TiO2 single crystals and nanoparticles," Nature Communications, vol. 8, no. 1, pp. 13–13, 2017.
49. J. Pascual, J. Camassel, and H. Mathieu, "Fine structure in the intrinsic absorption edge of TiO2," Physical Review B, vol. 18, no. 10, pp. 5606–5614, 1978.
50. W. Tian, T. Zhai, C. Zhang, S. L. Li, X. Wang, F. Liu, D. Liu, X. Cai, K. Tsukagoshi, D. Golberg, Y. Bando, Adv. Mater. 2013, 25, 4625.
51. Shaho M. Rasul; Dlear R. Saber; Shujahadeen B. Aziz. In: Results in Physics, Vol 38, Iss , Pp 105688- (2022).
52. M. Zhanhong; F. Ren; X. Ming; Y. Long; A. A. Volinsky Materials, 12 (2019), p. 196.
53. Z. Nabi; A. Kellou; S. Méçabih; A. Khalfi; N. Benosman Mater. Sci. Eng. B Solid-State Mater. Adv. Technol., 98 (2003), p. 104.
54. Ishchenko O, Rogé V, Lamblin G, Lenoble D, Fechete I. TiO 2 , ZnO, and SnO 2 -based metal oxides for photocatalytic applications: principles and development. C R Chim. 2021;24(1):103–24. http://dx.doi.org/10.5802/crchim.64.
n the content.